Synergy Between Lithium Plasma-Facing Component Coatings and the Snowflake Divertor Configuration in NSTX.

V. A. Soukhanovskii 1), J.-W. Ahn 2), M. G. Bell 3), R. E. Bell 3), D. A. Gates 3), S. Gerhardt 3), R. Kaita 3), E. Kolemen 3), H. W. Kugel 3), B. P. LeBlanc 3), R. Maqueda 4), A. McLean 2), J. E. Menard 3), D. Mueller 3), S. F. Paul 3), A. Y. Pigarov 5), R. Raman 6), T. Rognlien 1), A. L. Roquemore 3), D. D. Ryutov 1), S. A. Sabbagh 7), R. Smirnov 5), D. P. Stotler 3)

1) Lawrence Livermore National Laboratory, Livermore, CA, USA
2) Oak Ridge National Laboratory, Oak Ridge, TN, USA
3) Princeton Plasma Physics Laboratory, Princeton, NJ, USA
4) Nova Photonics, Inc., Princeton, NJ, USA
5) University of California at San Diego, La Jolla, CA, USA
6) University of Washington, Seattle, WA, USA
7) Columbia University, New York, NY, USA
Email address of main author: vlad@llnl.gov

Abstract. The studies of an innovative snowflake divertor (SFD) configuration and evaporated lithium wall and divertor coatings in the National Spherical Torus Experiment (NSTX) provide support to these plasma-material interface concepts as viable candidates for future high divertor heat flux tokamaks and spherical tokamak (ST) based devices for fusion development applications. Lithium coatings have enabled ion density reduction up to 50 % in NSTX via a significant reduction of wall and divertor recycling rates. Access to low core collisionality (at reduced density) is important for adequate neutral beam injection (NBI) current drive efficiency, and for understanding transport, stability, and non-inductive start-up and sustainment relevant to future ST-based facilities. With lithium, the outer SOL transport regime changed from the high-recycling, heat conduction-limited to the sheath-limited regime. A recycling coefficient of $R \sim 0.85$ and edge transport enhancement were inferred from interpretive two-dimensional multi-fluid edge transport modeling. The SFD configuration obtained in 0.8 MA 4-6 MW NBI-heated H-mode lithium-assisted discharges using a minimal set (two) of divertor coils, demonstrated good impurity control and divertor heat flux handling, as well as compatibility with H-mode confinement. A divertor plasma-wetted area, increased in the SFD by up to 90 %, as well as a longer connection length and a larger divertor volume, as compared to a standard divertor configuration, led to an increase in volumetric radiated power and a partial strike point detachment with an associated peak heat flux reduction by 50-90 %. The core carbon density and radiated power were also reduced by up to 75 %.

1. Introduction

A present vision of the plasma-material interface (PMI) for magnetic fusion energy (MFE) high-temperature plasma devices (tokamaks) is a poloidal magnetic X-point divertor. The divertor plasma-facing components (PFCs) must be able to withstand steady-state heat fluxes up to $q \simeq 10 \ \mathrm{MW/m^2}$, a limit imposed by the present day divertor material erosion and active cooling constraints. In addition, the divertor operation must be compatible with high-performance high-confinement (H-mode) core plasma as well as provide impurity control and hydrogenic fuel pumping capabilities. In order to reduce the power deposited in the divertor chamber, a number of solutions based on active techniques, e.g., impurity or D_2 seeded radiative divertors, field ergodization and strike point (SP) sweeping, and passive techniques, e.g., the number of divertors and divertor geometry, have been developed [1, 2]. These techniques aim to reduce the parallel heat flux $q_\parallel$ by volumetric power loss processes or scrape-off layer (SOL) power partitioning, and reduce the heat flux q_{div} deposited on the PFCs by increasing the plasma-wetted surface area. In large aspect ratio tokamaks, good progress has been made toward integrating the mentioned heat flux reduction techniques with impurity and density control solutions, e.g., cryopumping

for ion and helium ash removal and impurity entrainment in the SOL flow induced by deuterium puffing ("puff-and-pump") [1]-[6].

Spherical tokamaks (STs) impose even greater demands on divertor heat flux handling. The ST is viewed as a candidate concept for future fusion and nuclear science MFE devices [7, 8, 9]. Experiments in the National Spherical Torus Experiment (NSTX), a high-power density medium size ST ($R = 0.85$ m; $a = 0.65$ m) with graphite tile PFCs, have demonstrated the challenges of the inherently compact ST divertor: a large out/in SOL power ratio, a small divertor PFC area and reduced divertor volumetric (radiated power and momentum) losses. ITER-scale steady-state divertor peak heat fluxes $q_{pk} \leq 15$ MW/m^2 and $q_{\parallel} \leq 200$ MW/m^2 have been measured in $I_p = 1.0 - 1.2$ MA discharges heated by a 6 MW neutral beam injection (NBI) [10]-[12]. While a successful reduction of divertor q_{pk} to 0.5-3 MW/m^2 simultaneously with high (H-mode) core confinement has been demonstrated in NSTX with an additional divertor D_2 injection [11, 13], an integrated approach that combines divertor heat flux mitigation with density and impurity control is yet to be developed for the planned NSTX-Upgrade [14]. Access to low core collisionality ν (at $n_e \sim 0.5 - 0.7 \times n_G$ [7], where n_G is the Greenwald density) is important for adequate NBI current drive efficiency, and for understanding transport, stability, and non-inductive start-up and sustainment relevant to future ST-based facilities.
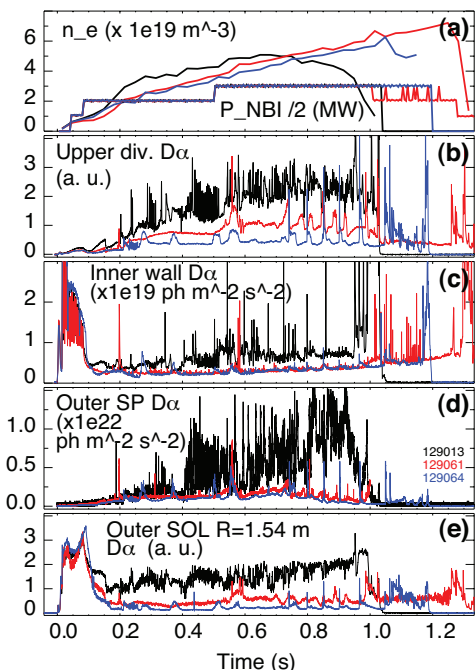
This paper reports on experimental studies of two novel PMI approaches in NSTX. Evaporated lithium PFC coatings were used for ion density pumping, while divertor peak heat flux reduction and impurity control were achieved with a snowflake divertor (SFD) configuration. These highly encouraging results provide further support to the SFD configuration and lithium-coated PFCs as viable PMI concepts for future MFE devices for fusion development applications.

2. Recycling, pumping and SOL transport with lithium coatings

Solid lithium coatings on graphite PFCs and liquid lithium PFCs are studied in NSTX for impurity and density control applications [15]-[17]. Experiments described in this section were conducted using two lithium evaporators that deposited solid lithium coatings over the lower divertor area [15]. Following the application of lithium PFC coatings, a number of performance modifications have been observed: in the core, decreases in the plasma density and inductive flux consumption, as well as increases in T_e, T_i, and the energy confinement time [16]; in the pedestal region, stability alteration leading to a reduction or elimination of edge localized modes (ELMs) [18, 19]. In this section, we describe SOL and divertor recycling and transport modifications induced by lithium coatings.

Figure 1: Time histories of (a) $\bar{n}_e$ and P_{NBI}; and D_α intensities in (b) Upper divertor, (c) Inner wall, (d) Lower divertor SP region, (e) outer SOL in the reference and two lithium-conditioned discharges (red - 190 mg of lithium, blue - 600 mg of lithium).

The experiment was conducted in 1 MA 4-6 MW NBI-heated H-mode discharges with strong shaping ($\kappa \sim 2.3; \delta \sim 0.85$) and $\delta r_{sep} \simeq -6$ mm [16]. We compare three similar discharges: a reference H-mode discharge without lithium, and two discharges with 190 mg and 600 mg of lithium evaporated in the NSTX vessel. The reference discharge had frequent, medium-size type I ELMs, whereas the discharges with lithium conditioning had few infrequent ELMs. The diagnostic systems used in these studies are described elsewhere [13].

Lithium atoms bind the incident plasma ions and neutral deuterium atoms, depending on the incident particle energy, up to a full 200-400 nm lithium coating thickness, by forming a

LiD compound. This gettering effect significantly reduces the recycled deuterium flux Γ_{recy}. Shown in Fig. 1 are the time traces of D_α intensities in the upper and lower divertors as well as on the inner wall and in the outer SOL midplane (MP). The flux Γ_{recy} is proportional to the D_α intensity via the atomic S/XB factor about 10-40 from a collisional-radiative model (as has been done in, e.g., [20]). A reduction in the entire poloidal Γ_{recy} profile by 50-100 % was evident in the lithium discharges. This reduction was observed not only in the lower divertor, where lithium was evaporated, but also on other PFCs, suggesting that plasma re-deposition of lithium occurred. Similar reductions were observed in the neutral pressure measurements in both divertors and at the midplane. Lithium coatings showed a cumulative effect on recycling and neutral pressure, i.e. a thicker lithium coating led to a higher degree of the Γ_{recy} reduction.

Figure 2: Relative local recycling coefficients in the discharge with 190 mg lithium normalized to those in the discharge without lithium, at 0.45 s and 0.77 s, at four poloidal locations.

Plasma density evolution strongly depends on the PFC recycling coefficient. The local recycling is defined as $R = \Gamma_{recy}/\Gamma_i$, where Γ_i is the ion flux. In the absence of lithium, $R \simeq 0.95 - 0.99$ is realized in NSTX [21] and in high-recycling tokamak divertors [1]. Using Γ_i measured by tile-mounted Langmuir probes at a few discrete poloidal locations we calculated the effect of lithium on local R's. Although the absolute R's are desirable for input in 2D edge transport codes, uncertainties in local S/XB factors and field line angles in respect to the probe tips precluded the desired accuracy [20]. Instead, we compare trends in relative R coefficients, as shown in Fig. 2. After the application of lithium, R was reduced in the upper divertor, on the MP inner wall and in the far SOL in the lower divertor. However, in the near-SOL and the SP regions, R was either higher or marginally reduced, suggesting that lithium may be melted in the SP region (thus adding to the recycling flux by releasing deuterium), and even evaporated from the SP region by the end of the discharge.

With the reduced PFC recycling fluxes, a significant, up to 50 %, steady-state reduction in core ion inventory (and density) was observed. Shown in Fig. 3 are the time histories of core N_e, N_C and N_{D+} inventories calculated from the measured $n_e(r)$ and $n_C(r)$ profiles. The ion inventory was calculated under the assumption that carbon was a dominant plasma impurity, according to $N_d(t) = N_e(t) - 6 N_C(t)$. The increased amount of deposited lithium, while having a cumulative effect on PFC recycling, marginally affected the total ion inventory (and ion density). We note that the gas fueling rate was increased by 20-40 % in the discharge with more lithium deposition, suggesting a cumulative effect on the pumping rate as well. The core N_e (and n_e) in discharges with lithium, while being lower in the initial phase of the discharge, eventually increased and exceeded that without lithium. As the particle inventory balance in Fig. 3 indicated, a significant contribution to n_e came from carbon ionization. Carbon accumulated in the ELM-free H-mode discharges with lithium conditioning, as did other metallic impurities, leading to increased $Z_{eff} \sim 4 - 5$ and a much higher
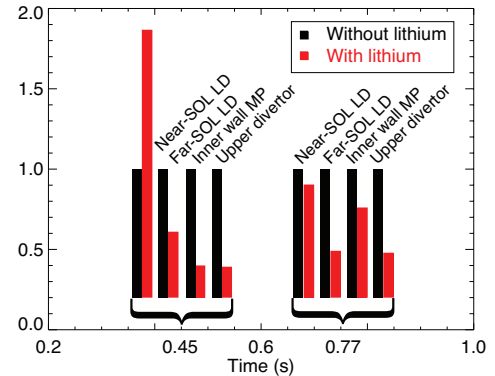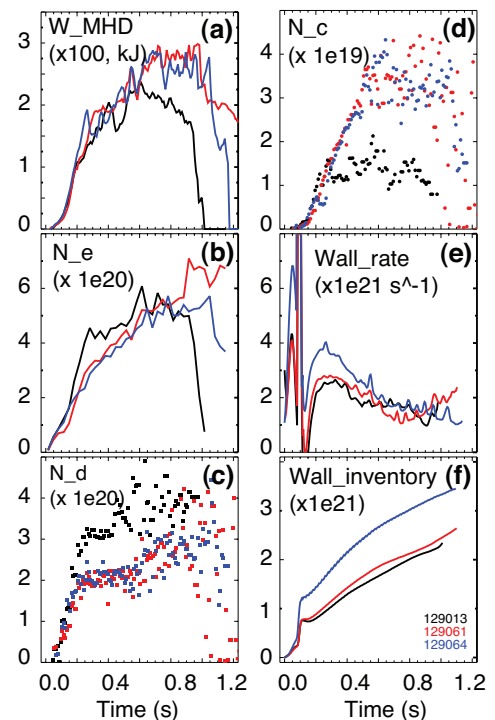
Figure 3: Time histories of (a) Plasma stored energy; Core particle inventories: (b) N_e; (c) N_{D+}; (d) N_C; (e) Wall loading rate; (f) Wall inventory for the discharges as in Fig. 1.

core $P_{rad} \sim 1 - 3$ MW. Lithium, however, was effectively screened out from the core plasma, with a typical $n_C(0)/n_{Li}(0) \simeq 100$, as indicated by lithium core density measurements [16].

Further insights on lithium pumping were obtained from a particle balance equation that was used to calculate the net wall loading rate and the net cumulative wall inventory from the measured N_{D+}, gas and pumping sources and sinks [20, 22, 23]. Time histories of these quantities shown in Fig. 3e-f indicate that (1) lithium coatings provided continuous pumping over an entire discharge duration; however, they appeared to reach a lower pumping state toward the discharge end; (2) cumulative lithium coatings provided a higher pumping rate; (3) the wall appeared to be in a pumping state far from saturation, evident from the positive wall loading rate and the wall inventory continuously increasing throughout a discharge.

Figure 4: *Measured T_e and n_e at an estimated R_{sep} location in respect to divertor regime boundaries defined in terms of ν_e^* for the discharges as in Fig. 1.*

We now discuss the modifications observed in the SOL and divertor transport regime caused by lithium conditioning. Before the application of lithium, the outer SOL transport regime was in the high-recycling, heat flux conduction-limited state (e.g., [11, 24]). The reduction in recycling led to the sheath-limited regime with convective heat transport. Shown in Fig. 4 are the SOL heat transport boundaries in terms of parallel thermal electron collisionality $\nu_e^* = l_c/\lambda_e$ (where λ_e is the electron mean free path and $l_c \simeq 10$ m is a typical connection length). The T_e, n_e data measured by the Thomson scattering system for estimated separatrix lo-

Figure 5: *Top panel: Radial profiles of (a) measured and modeled n_{D+}; (b) measured and modeled T_i; (c) Heat and particle transport coefficients in the UEDGE model for the reference and lithium discharges. Bottom panel (d)-(f): Modeled MP and divertor quantities as a function of albedo (recycling coefficient).*

cations are overlaid. Without lithium, $\nu_e^* \sim 10 - 30$ were typical for lower NBI power, and $\nu_e^* \sim 3 - 10$ were typical for higher NBI power and during ELM events. Application of lithium led to lower SOL n_e and higher T_e, thus shifting the operating regime to lower SOL collisionalities $\nu_e^* \sim 1 - 10$. The boundary between the sheath-limited and the conduction-limited regimes was assumed to be about $\nu_e^* \sim 10$ [25]. The inner divertor SP, typically detached in NSTX discharges [24, 26], re-attached, as the inner divertor n_e was reduced from $3 - 5 \times 10^{20}$ to $0.6 - 2 \times 10^{20}$ m^{-3} [27]. This was also accompanied by a reduction in MARFE activity in the inner SOL region, as well as a 50-80 % reduction in C II and C III emission and total divertor radiation.

Edge transport modifications due to lithium coatings were studied using the 2D multi-fluid edge transport code UEDGE [28] with kinetic flux limits on a mesh extending from the pedestal region to the far SOL. Both Li and C impurities were included. The diffusive-convective poloidally-varying radial transport model was used [29]. Further details on the transport and recycling surface models, as well as comparison with the data, are given in Refs. [30, 31]. In this paper we highlight two results from the modeling. First, after matching of the MP $n_C, n_{D+}, n_e, T_e, T_i$ and D$_\alpha$ profiles (examples shown in Fig. 5a-b), as well as divertor D$_\alpha$ profiles, Lamgmuir probe I_{sat} and neutral pressure measurements for the reference discharge and for the discharge with 160 mg lithium, the transport coefficients shown in Fig. 5c were concluded from the interpretive modeling. Enhanced radial transport through the edge was obtained in the dis-
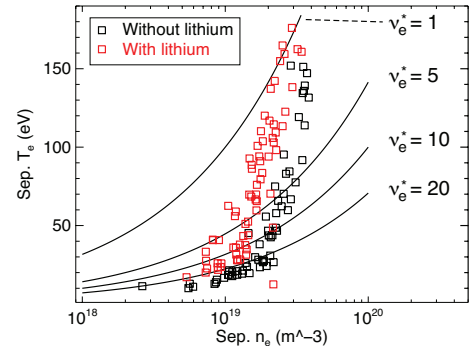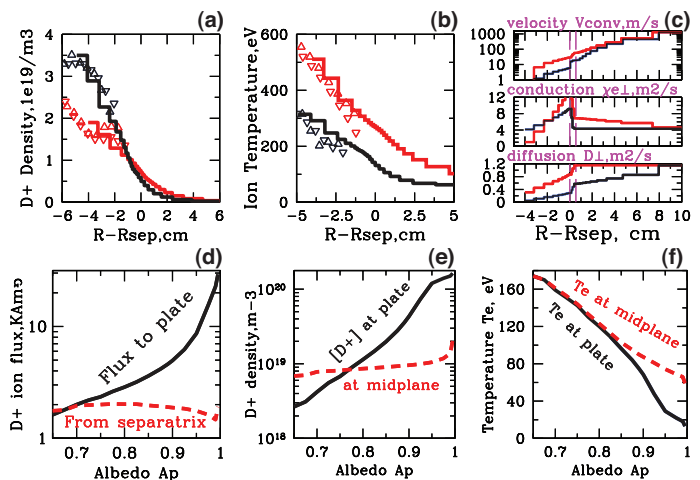
charge with lithium, as the radial deuteron diffusion and convective velocity coefficients, as well as electron heat conduction were increased. A large inward neoclassical pinch was characteristic of the impurity transport (not shown). Second, the model was used to study the particle flux, T_e and $n_e(n_i)$ trends in the SOL and divertor as functions of the recycling coefficient, as shown in Fig. 5d-f. The sheath-limited SOL regime with similar MP and divertor ion fluxes, no divertor density "amplification" inherent to the conduction-limited regime, and similar MP and divertor T_e were found at about $R = 0.80 - 0.85$, suggesting that the recycling coefficients as low as these were characteristic of the NSTX discharges with lithium.

Figure 6: (a) Medium $\delta \sim 0.65$ standard divertor and (b) SFD-like configurations. Flux surfaces separated by 2 mm in the MP are shown. Null points are indicated by crosses. Also shown are the divertor Langmuir probe, neutral pressure Penning gauge, and divertor bolometer chord.

3. "Snowflake" divertor configuration

In this Section, we report on the recent NSTX experimental results that fully confirmed the theoretically predicted novel "snowflake" divertor configuration properties [32]. While the conventional poloidal magnetic X-point divertor concept has existed for three decades, several theoretical ideas proposing novel divertor geometries with favorable PMI characteristics have emerged recently [32]-[34]. The SFD configuration [32], [35]-[37] uses a second-order poloidal field null created by merging, or bringing close to each other, two first-order poloidal field null points (X-points) of a standard two-coil divertor configuration. A poloidal cross-section of the obtained magnetic flux surfaces with a hexagonal null-point has an appearance of a snowflake. The poloidal field B_p increases with distance as r^2 in the vicinity of the second order null (vs r in the vicinity of a first order null in the standard divertor), leading to (1) an increased divertor magnetic flux expansion f_m; (2) an increased plasma-wetted area A_{wet}; (3) an increased X-point connection length L_x [35, 37]. The latter increases the heat diffusive loss into the private flux region, as well as the divertor volume available for impurity radiation and ion momentum losses. The SFD magnetic equilibria have been simulated for several tokamaks with existing divertor coils [36, 37]. The SFD has been realized in the TCV tokamak using a set of six divertor coils [38].

Magnetic control is critical for the two-coil SFD concept, since a second-order null configuration is topologically unstable [32]. Two stable SFD-like configurations can be realized in practice: a SFD-plus, where the divertor coil currents slightly exceed those of the ideal SFD case, and a SFD-minus, where the corresponding divertor coil currents are slightly lower [32]. In the NSTX experiment, the plasma control system (PCS) was used to hold the SP positions for the SFD configuration modeled with a predictive free-boundary axisymmetric Grad-Shafranov equilibrium code [39]. The SFD-like configurations were obtained in a number of discharges for periods of 50-150 ms. The SFD discharge to be discussed below had five periods with the SFD-minus-like (Fig. 6b), and one with the SFD-plus-like (not shown) configurations.

Magnetic and plasma characteristics of the SFD were studied in discharges with $I_p = 0.8$ MA, $B_t = 0.4$ T, 4-6 MW of NBI heating, and 80-100 mg of lithium evaporated on PFCs per discharge. Two H-mode discharges with similar shaping ($\kappa \sim 1.9 - 2.0$ and $\delta \sim 0.6 - 0.7$) and SOL power $P_{SOL} \simeq 3$ MW, but with different divertor configurations (the standard divertor vs the SFD-minus, shown in Fig. 6a-b) will be compared.

The experimental magnetic equilibria reconstructed with the Grad-Shafranov codes EFIT and LRDFIT confirmed the magnetic geometry properties of the SFD predicted by the analytic two-coil SFD theory [32, 35]. Divertor geometries of the standard and SFD discharges are
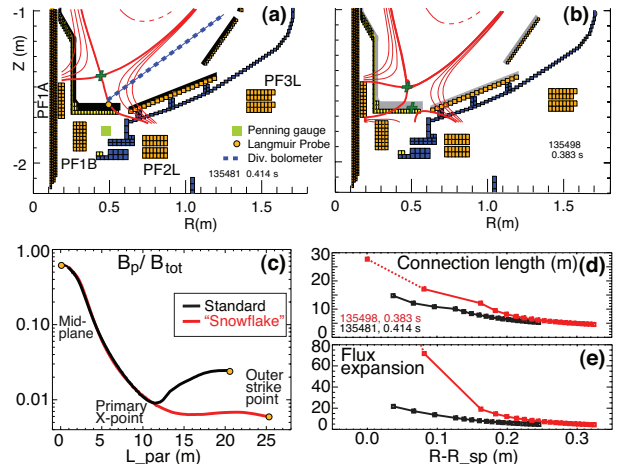
compared in Fig. 6. The presence of a secondary null-point in the SFD reduced B_p/B_{tot} in the divertor separatrix region by up to 90 %, as shown in Fig. 6c. This increased both L_x by up to 50 % and f_m (as well as A_{wet}) in the outer SP region by up to 90 %. The radial divertor profiles of both L_x and f_m in Fig. 6d-e show that the geometry was modified in the separatrix region ($\Delta = 2 - 3$ mm when mapped to MP using f_m), while similar magnetic properties were noted at large distances from the nulls in both discharges.

The SFD did not cause any degradation in core confinement and was compatible with H-mode operation (Fig. 7a). In the standard divertor discharge, ELMs were suppressed due to lithium conditioning [18], thus leading to impurity accumulation with $Z_{eff} \leq 4$ and radiated power $P_{rad} = 1 - 3$ MW after 0.5 s [40]. The SFD discharge in contrast showed exceptional impurity screening properties: the core carbon inventory N_c (as well as P_{rad}) was reduced by up to 75 % leading also to a 10-15 % reduction in n_e (Fig. 7c-d). The similarity of the carbon density profiles (up to a scaling factor) suggested a carbon source reduction in the SFD.

Divertor measurements in the SFD showed the commonly-observed characteristics of divertor detachment [1, 2, 13]: an increase in divertor radiated power and electron-ion recombination rates, a loss of parallel pressure balance, and as a result, a decrease of heat and particle fluxes to the plate. A good correlation was observed between the SFD periods, defined by the inter-null distance $d \leq 20$ cm shown in Fig. 7e, on one hand, and the increases in the outer SP divertor D_α intensity due to recombination, increases in neutral pressure, reduction of the SP Langmuir probe I_{sat} (anti-correlated with the SP region D_α), significant drops in the divertor heat flux averaged over the radial region $\Delta = 15$ cm adjacent to the outer SP, on the other hand, as shown in Fig. 7e-i. While the heat flux measurements were uncalibrated due to lithium coatings on divertor surfaces, typical $q_{pk} = 4 - 6$ MW/m^2 have been measured in similar standard divertor discharges. The averaged divertor heat flux was reduced in the SFD discharges by up to $30 - 40$ % due to increased divertor radiated power. The divertor bolometer signal indicative of divertor P_{rad} showed a 50 % increase in the SFD vs the standard divertor (Fig. 7j). Divertor peak heat fluxes q_{pk} were reduced by up to 90 % in the detached separatrix region ($\Delta = 2 - 3$ mm as mapped to MP with f_m taken into account), as shown in Fig. 7k. Taking the MP SOL width as $\lambda_{q_\parallel} \sim 6 - 7$ mm [12]. we conclude that a large fraction of divertor heat was exhausted through volumetric processes in the SFD. In the attached SOL region at $R_{div} - R_{SP} \geq 0.15$ m, similar divertor heat fluxes were measured in the SFD and the standard divertor.

Divertor detachment is often accompanied by an increase in the electron-ion recombination rate, a process of volumetric ion momentum removal. The three-body recombination rate R is highly sensitive to local divertor T_e, n_e as $R \sim n_e^3$ and $R \sim T_e^{-4.5}$. The deuterium high-n Balmer series transitions are indicative of recombination rate R and local T_e, n_e [41, 42], as (1) their upper levels n are populated by three-body recombination only; (2) the atomic level populations are governed by the Saha-Boltzman distribution; and (3) their spectral line Stark broadening is due to electron and ion electric micro-fields. In the SFD discharges, spatially resolved Balmer spectra showed a formation of a large volume recombination region, as indicated by the B10 line emission profiles in Fig. 7L. The Balmer line intensities and shapes were modeled using the radiation transport and collisional-radiative code CRETIN [43]. The spectra were highly sensitive to both T_e and n_e, and the model implied that average $T_e \simeq 0.8 - 1.1$ eV and $n_e \simeq 2 - 7 \times 10^{20}$ m^{-3} were characteristic of the detachment zone (Fig.7m). A comparison of the inferred electron pressure in the SP region $p_e = n_e T_e \sim 25 - 80$ Pa to the measured MP pressure $p_e \sim 50 - 120$ Pa confirmed a pressure decrease from MP to target in the SFD.

The described SFD configuration was obtained with two divertor coils and without null-point position control. The development of the two-coil SFD concept is important for next-step high-power fusion devices that are likely to have few magnetic coils due to engineering and neutron constraints. We are presently implementing the real-time tracking and control of the second null-point in the NSTX PCS in order to maintain the two-coil SFD for an entire discharge
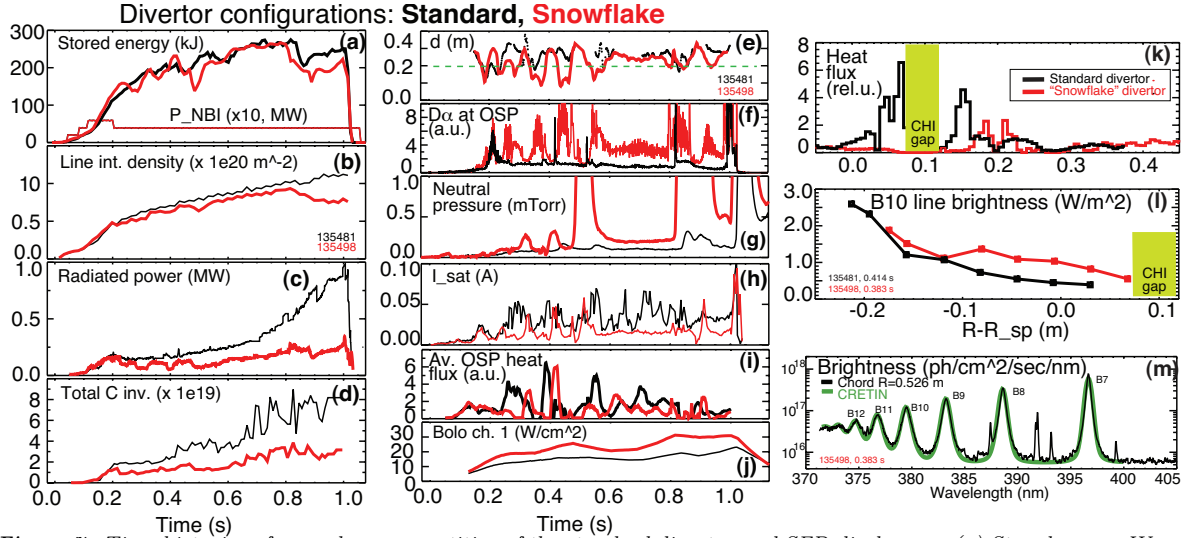
Figure 7: *Time histories of core plasma quantities of the standard divertor and SFD discharges: (a) Stored energy W_{MHD} and P_{NBI}; (b) $\int n_e dl$; (c) Core P_{rad}; (d) N_C; (e) null-point separation d; (f) Divertor outer SP D_α; (g) Divertor neutral pressure; (h) Divertor probe I_{sat}; (i) Average divertor heat flux; (j) Divertor bolometer signal; (k) Relative heat flux profiles; (l) Balmer B10 $\lambda = 379$ nm line brightness profiles; (m) Divertor Balmer spectrum measured at $R - R_{SP} \simeq 0.03$ m in the SFD and modeled with CRETIN code using $T_e = 1.05$ eV and $n_e = 4 \times 10^{20}$ m^{-3}.*

duration. Recently, we have also obtained a steady-state SFD-minus configuration for up to 0.6 s duration using three divertor coils. The third coil PF1B (Fig. 6a) was operated in a reversed polarity w.r.t. to the PF1A and PF2L coils, maintaining a region of reversed-sign magnetic flux for configuration stability.

4. Discussion and summary

Steady-state operation of next-step tokamak and ST-based fusion devices is likely to push the limits of the present PMI designs. Recent experimental studies of new approaches to impurity control, density pumping and divertor heat flux mitigation in NSTX using evaporated lithium PFC coatings and the "snowflake" divertor configuration provide support for these PMI concepts as viable candidates for future fusion development applications.

While the SFD configuration is conceptually suitable for a reactor-type device, the NSTX lithium coating study is a first step toward a lithium-based PMI interface. The lithium PFC coatings provide a high-conductance pumping solution compatible with the open NSTX divertor geometry and high magnetic flux expansion configurations. For the near-term NSTX and NSTX-U programs, this solution may be sufficient in order to establish and study high-β_N low collisionality plasmas with high-non-inductive current fraction [44]. Since peak divertor heat fluxes up to 24 MW/m^2 are projected for NSTX-U [12], the SFD in combination with lithium coatings would address both the particle and heat flux control needs.

One outstanding issue with lithium-coated PFC operation in NSTX is impurity control. Even though higher sputtering rates are expected in the sheath-limited divertor regime, only co-deposited carbon is expected to be sputtered since graphite PFCs are coated with lithium. Preliminary spectroscopic measurements indicated that the wall and divertor carbon fluxes did not increase with lithium conditioning, thus the neoclassical inward pinch and ELM-free operation appear to be the main causes of the impurity accumulation. In contrast, the SFD discharges demonstrated good impurity screening. In the partially detached divertor SP region with $T_e \leq 1 - 2$ eV, a significant reduction of divertor physical and chemical sputtering rates, as well as an improved impurity entrainment in a hydrogenic plasma flow are expected [11, 13, 45], to be confirmed in the forthcoming SFD experiments in NSTX.

The SFD configuration in combination with lithium coatings provide an interesting case for divertor regime studies. Typically, tokamak SOL collisionality-dependent heat transport

regimes are modified by changing SOL T_e and n_e, as, e.g., in the case with low-recycling lithium coatings or a partially-detached divertor with gas puffing (e.g., [11]). In the SFD, a sheath-limited outer SP region (emulating the physics of high-heat flux divertors of future facilities [8]) was transformed to a partially-detached SP by increasing the connection length L_x, which in turn led to increases in the collisionality ν_e^*. The pumping provided by lithium coatings apparently also prevented an X-point MARFE formation in the separatrix region with the increased L_x.

In summary, lithium coatings have enabled ion density reduction up to 50 % in NSTX. The SFD configuration was obtained for the first time with a minimal number (two) of divertor coils; it resulted in a significant reduction of divertor q_{div} and $q_\parallel$ leading to a partial detachment of the outer strike point; it proved to be compatible with H-mode core confinement while demonstrating favorable impurity screening properties.

References

[1]   ITER Physics Expert Group on Divertor et al., Nucl. Fusion **39** (1999) 2391.
[2]   LOARTE, A. et al., Nucl. Fusion **47** (2007) S203.
[3]   TAKENAGA, H. et al., Nuclear Fusion **41** (2001) 1777.
[4]   PETRIE, T. et al., Nucl. Fusion **46** (2006) 57.
[5]   PETRIE, T. et al., Nucl. Fusion **49** (2009) 065013.
[6]   NAKANO, T. et al., Nucl. Fusion **48** (2008) 085002.
[7]   PENG, Y.-K. et al., Plasma Phys. Control. Fusion **47** (2005) 263.
[8]   CANIK, J. et al., J. Nucl. Mater. **390-391** (2009) 315.
[9]   GOLDSTON, R. et al., in *Fusion Energy 2008 (Proc. 22nd Int. Conf. Geneva, 2008)*, Paper FT/P3-12, Vienna:IAEA.
[10]   MAINGI, R. et al., Plasma Phys. Control. Fusion **45** (2003) 657.
[11]   SOUKHANOVSKII, V. et al., Nucl. Fusion **49** (2009) 095025.
[12]   GRAY, T. K. et al., Paper EXD/P3-13, in *These Proceedings*.
[13]   SOUKHANOVSKII, V. A. et al., Phys. Plasmas **16** (2009) 022501.
[14]   MENARD, J. et al., in *Proc. 37th EPS Conf. on Plasma Phys.*, volume 34F of *Europhys. Conf. Abstr.*, pages P–2.106, Dublin, Ireland, 2010.
[15]   KUGEL, H. W. et al., Phys. Plasmas **15** (2008).
[16]   BELL, M. et al., Plasma Phys. Control. Fusion **51** (2009) 124054.
[17]   KUGEL, H. W. et al., Paper FTP/3-6Ra, in *These Proceedings*.
[18]   MAINGI, R. et al., Phys. Rev. Lett. **103** (2009) 075001.
[19]   MAINGI, R. et al., Paper EXC/2-2, in *These Proceedings*.
[20]   SOUKHANOVSKII, V. et al., J. Nucl. Mater. **390-391** (2009) 516.
[21]   MAINGI, R. et al., Nucl. Fusion **45** (2005) 264.
[22]   MAINGI, R. et al., Nucl. Fusion **36** (1996) 245.
[23]   SOUKHANOVSKII, V. et al., J. Nucl. Mater. **313-316** (2003) 573.
[24]   SOUKHANOVSKII, V. et al., J. Nucl. Mater. **337-339** (2005) 475.
[25]   STANGEBY, P. C., *The plasma boundary of Magnetic Fusion Devices*, IoP, Bristol, 2000.
[26]   SOUKHANOVSKII, V. et al., Phys. Plasmas **16** (2009) 022501.
[27]   SCOTTI, F. et al., J. Nucl. Mater. **at press** (2011).
[28]   ROGNLIEN, T. D. et al., J. Nucl. Mater. **196-198** (1992) 347.
[29]   PIGAROV, A. et al., J. Nucl. Mater. **337-339** (2005) 371.
[30]   SMIRNOV, R. et al., Contrib. Plasma Phys. **50** (2010/05/) 299.
[31]   PIGAROV, A. Y. et al., Phys. Plasmas, to be submitted (2010).
[32]   RYUTOV, D., Phys. Plasmas **14** (2007) 64502.
[33]   KOTSCHENREUTHER, M. et al., Phys. Plasmas **14** (2007) 72502.
[34]   VALANJU, P. et al., Phys. Plasmas **16** (2009) 056110.
[35]   RYUTOV, D. et al., Phys. Plasmas **15** (2008) 092501.
[36]   RYUTOV, D. et al., in *Fusion Energy 2008 (Proc. 22nd Int. Conf. Geneva, 2008)*, Paper IC/P4-8, Vienna:IAEA.
[37]   UMANSKY, M. et al., Nucl. Fusion **49** (2009) 075005.
[38]   PIRAS, F. et al., Plasma Phys. Control. Fusion **51** (2009) 055009.
[39]   KOLEMEN, E. et al., Nucl. Fusion **50** (2010) 105010.
[40]   CANIK, J. et al., Phys. Rev. Lett. **104** (2010) 045001.
[41]   BENGTSON, R. D. et al., Phys. Rev. A (1970) 532.
[42]   GRIEM, H. R., Phys. Scripta **T83** (1999) 142.
[43]   SCOTT, H., J. Quant. Spectrosc. Radiat. Transf. **71** (2001) 689.
[44]   GERHARDT, S. P. et al., Paper IC/P7-13, in *These Proceedings*.
[45]   WHYTE, D. et al., Nuclear Fusion **41** (2001) 1243.